Accepted Manuscript

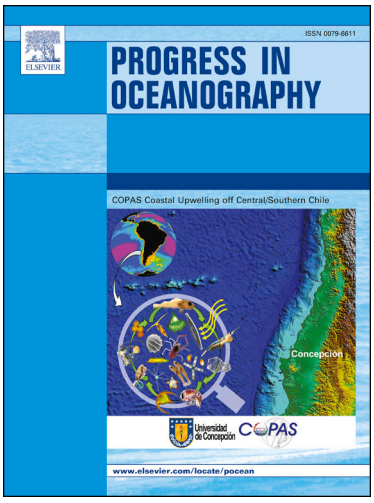

Internal tides in a dendritic submarine canyon

Tahmeena Aslam, Rob A. Hall, Stephen R. Dye

PII: S0079-6611(17)30249-5
DOI: https://doi.org/10.1016/j.pocean.2017.10.005
Reference: PROOCE 1861

To appear in: *Progress in Oceanography*

Accepted Date: 12 October 2017

Please cite this article as: Aslam, T., Hall, R.A., Dye, S.R., Internal tides in a dendritic submarine canyon, *Progress in Oceanography* (2017), doi: https://doi.org/10.1016/j.pocean.2017.10.005

This is a PDF file of an unedited manuscript that has been accepted for publication. As a service to our customers we are providing this early version of the manuscript. The manuscript will undergo copyediting, typesetting, and review of the resulting proof before it is published in its final form. Please note that during the production process errors may be discovered which could affect the content, and all legal disclaimers that apply to the journal pertain.

ACCEPTED MANUSCRIPT

Internal tides in a dendritic submarine canyon

Tahmeena Aslam[a,b], Rob A. Hall[a,*], Stephen R. Dye[a,b]

[a] *Centre for Ocean and Atmospheric Sciences, School of Environmental Sciences, University of East Anglia, Norwich Research Park, Norwich, NR4 7TJ, UK*
[b] *Centre for Environment Fisheries and Aquaculture Science, Pakefield Road, Lowestoft, Suffolk, NR33 0HT, UK*

Abstract

Submarine canyons are a common geomorphological feature along continental slopes worldwide and often found to be 'hotspots' of internal tide activity. However, the majority of well-studied submarine canyons are simple linear incisions or have meandering morphology; internal tide energetics in branching (dendritic) canyons has not previously been investigated. Here we present a high-resolution (500-m) numerical modelling study of the internal tide within Whittard Canyon, a large, dendritic submarine canyon system that incises the Celtic Sea continental slope. A modified version of the Princeton Ocean Model is used to simulate the M_2 (semidiurnal) internal tide in the Whittard Canyon region, verified against a hydrographic dataset collected by an autonomous ocean glider. Much of the internal tide energy entering Whittard Canyon originates to the southeast, along the Celtic Sea shelf break. Internal tide generation also occurs within the canyon itself, but is in part compensated by areas of negative energy conversion. Depth-integrated internal tide energy fluxes exceed 8 kW m^{-1} in the eastern limb of the canyon. The internal tide is topographically steered through the major limbs and along-canyon energy flux is bottom intensified, suggesting topographic focusing. The down canyon extent of bottom intensification closely corresponds to the point that along-canyon slope becomes near-critical to the semidiurnal internal tide. Energetically, the multiple limbs of Whittard Canyon behave differently, some are net sources of internal tide energy whilst others are net sinks. Internal tide energy dissipation also varies between the canyon limbs; bulk dissipation rates are 2.1-7.7 $\times$ 10^{-8} W kg^{-1}. In addition, the effect of bathymetric resolution on internal tide generation and propagation is investigated by progressively smoothing the model domain. Decreasing the bathymetric resolution reduces internal tide generation and energy dissipation in both Whittard Canyon and the model domain as a whole, however, internal tide energy flux into the canyon is not consistently changed. At least 1.5-km resolution bathymetry is required to adequately resolve the semidiurnal internal tide field in this region of complex topography.

Keywords: Internal tides, Submarine canyons, Princeton Ocean Model, Celtic Sea, Whittard Canyon

1. Introduction

Internal tides are a common hydrodynamic feature of submarine canyons worldwide (e.g., Shepard et al., 1974; García Lafuente et al., 1999; Wain et al., 2013). These large-amplitude internal gravity waves with tidal frequencies are either generated locally, by barotropic (surface) tidal currents across the sloping canyon bathymetry (Bell, 1975; Baines, 1982), or are generated remotely and trapped within the canyon by reflection from the typically steep walls (Gordon and Marshall, 1976) and gently sloping floor (Hotchkiss and Wunsch, 1982). Dissipation of internal tides within canyons is thought to be an important global sink of internal wave energy (Waterhouse et al., 2017) and may drive local biogeochemical fluxes (Kunze et al., 2002).

The majority of well-studied submarine canyons can be approximated as linear incisions, for example Hydrographers (Wunsch and Webb, 1979), Ascension (Gregg et al., 2011) and Congo (Vangriesheim et al.,

*Corresponding author
Email address: robert.hall@uea.ac.uk (Rob A. Hall)

ACCEPTED MANUSCRIPT

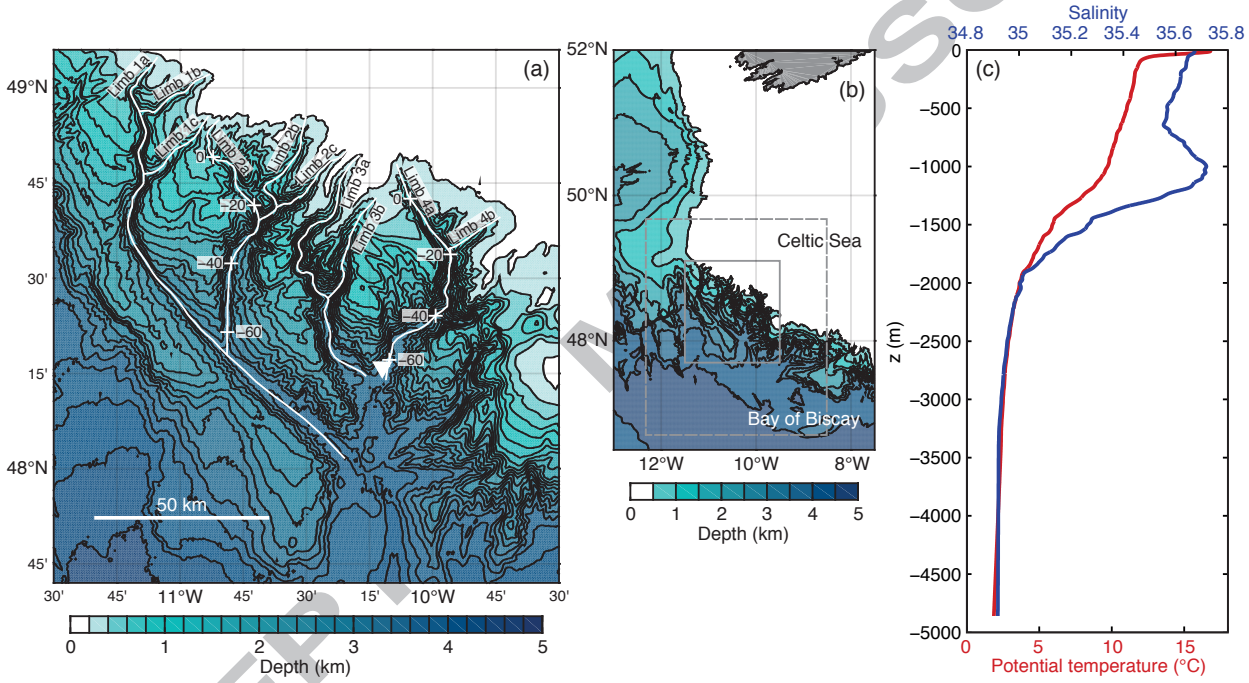

Figure 1: (a) Bathymetry of the Whittard Canyon system (INFOMAR-GEBCO, 200-m contour interval) showing the location and naming convention of the major and minor canyon limb thalwegs. For Limbs 2a and 4a, distance along the thalweg from the 1000-m isobath is marked with a cross at 20-km intervals. The white triangle is the location of the CTD cast used to initialise the numerical model. (b) Bathymetry of the Celtic Sea continental slope (GEBCO, 500-m contour interval) showing the location of the Whittard Canyon system (solid grey box) and the model domain (dashed grey box). (c) Potential temperature and salinity profiles used to initialise the model.

ACCEPTED MANUSCRIPT

2009) Canyons, or have sinuous, meandering morphology, for example Monterey (Kunze et al., 2002), Gaoping (Lee et al., 2009) and Nazaré (Masson et al., 2011) Canyons. Branching (dendritic) canyons have received less attention despite the fact that this morphological type is common worldwide (Harris and Whiteway, 2011). Specifically, the energetics of internal tides in dendritic canyons has not previously been investigated. Here we present the first numerical modelling study of internal tides in a dendritic submarine canyon: the Whittard Canyon system that incises the Celtic Sea continental slope.

Most previous studies of Whittard Canyon have focused on biological and sedimentological processes (see Amaro et al., 2016, for a review). The steep canyon walls, sections of which are vertical or overhanging, provide a solid substrate for the development of cold-water coral communities (Huvenne et al., 2011) and habitats for a diverse variety of benthic fauna (Johnson et al., 2013; Robert et al., 2015). On gentler slopes, sediment is resuspended by energetic hydrodynamics, forming benthic and intermediate nepheloid layers (density layers with high concentrations suspended particulate matter and organic material) that have been observed in several of the canyon's limbs (Wilson et al., 2015b). The physical oceanography of Whittard Canyon has received less attention (Johnson et al., 2013; Wilson et al., 2015b; Porter et al., 2016) and the internal tide field is essentially unknown. Hall et al. (2017) observed an 80-m amplitude semidiurnal internal tide in the eastern limb of the canyon using an autonomous ocean glider, but no tide-resolving hydrographic observations have been made in the other canyon limbs.

In the wider region, internal tides have previously been observed in the Bay of Biscay (e.g., Pingree et al., 1986; New, 1988) and Celtic Sea (e.g., Holt and Thorpe, 1997; Green et al., 2008; Sharples et al., 2009; Inall et al., 2011; Hopkins et al., 2014). High-resolution numerical models have also been used investigated how the internal tides generated at the Celtic Sea shelf break radiate onto the shelf (Vlasenko et al., 2014), into the Bay of Biscay (Vlasenko and Stashchuk, 2015), and are focused into Petite Sole Canyon (part of Dangeard Canyon; Vlasenko et al., 2016). Following this recent work, the aim of the present study is to investigate the generation and propagation of the semidiurnal internal tide around Bernot Spur and within Whittard Canyon. In Section 2, the configuration of the numerical model and diagnostics are described. In Section 3, the model output is verified against an observational hydrographic dataset. Internal tide generation and propagation through the canyon limbs is described in Section 4 and an energy budget for the upper reaches of the canyon constructed in Section 5. In Section 6, the effect of bathymetric resolution on internal tide generation and propagation is investigated and in Section 7 the implications of internal tide activity on nepheloid layer generation are discussed. Key results of the study are summarised in Section 8.

The Whittard Canyon system comprises of several multi-branched limbs so to identify individual limbs we use the naming convention shown in Figure 1a. The four major canyon limbs are numbered 1-4 (west to east). The thalweg[1] along each major limb is given the suffix 'a' and the thalwegs along the minor canyon limbs, those branching from the major limbs, are given the suffixes 'b' and 'c' (west to east).

2. Numerical model setup

A modified version of the Princeton Ocean Model (POM; Blumberg and Mellor, 1987) is used to simulate the M_2 (semidiurnal) internal tide in the Whittard Canyon region. POM is a three-dimensional, nonlinear, hydrostatic, free-surface, finite-difference, primitive equation model employing a sigma coordinate system in the vertical direction. The sigma coordinate system results in terrain-following vertical levels (following both the bathymetry and the free surface) that are evenly spaced through the water column. This provides good resolution of the surface and bottom boundary layers, the latter is important for this application as across-slope velocity is an important component of internal tide generation (Carter et al., 2012). The model has previously been used to simulate the internal tide field over the Hawaiian Ridge (Carter et al., 2008), Mid-Atlantic Ridge (Zilberman et al., 2009), within Monterey Canyon (Carter, 2010; Hall and Carter, 2011; Hall et al., 2014), and the Faroe-Shetland Channel (Hall et al., 2011).

The model domain extends from 12°19.4' W, 46°42.3' N to 8°30.6' W, 49°40.5' N (Fig. 1b) with 500-m horizontal resolution; fifty-one sigma levels are used. The simulation is run for 32 M_2 tidal cycles (16.56

[1]The thalweg of a canyon limb is the line that connects the deepest points of a series of bathymetric cross-sections along the length of the limb.

ACCEPTED MANUSCRIPT

days) from a quiescent state with vertically varying, but horizontally uniform, stratification. M_2 harmonic analyses are performed over the last 11 tidal cycles. Domain size and run length sensitivity tests have been performed; increasing the size of the model domain and increasing the length of the simulation both have limited effect on internal tide energetics in the Whittard Canyon region.

The bathymetric grid (Fig. 1a) is derived from the Integrated Mapping for the Sustainable Development of Ireland's Marine Resources programme 18 arc-second grid (INFOMAR, http://www.infomar.ie) and the General Bathymetric Chart of the Oceans 2014 30 arc-second global grid (GEBCO, http://www.gebco.net). Both data sources are interpolated onto a uniform, 500-m grid. The higher resolution INFOMAR bathymetry only covers the area of Whittard Canyon within Irish waters, so GEBCO data are used to fill the gaps.

The initial potential temperature and salinity profiles (Fig. 1c) are taken from a CTD cast over the abyssal plain close to the mouth of Whittard Canyon (10°11.9' W, 48°15.9' N) on 12 July 2009. These profiles are linearly extrapolated to the maximum depth within the model domain (4860 m) and smoothed using a 25-point gaussian tapered window running mean. Fifty-one evenly spaced sigma levels result in a vertical resolution of less than 1 m at some locations on the shelf and up to 97 m over the abyssal plain.

The model is forced at the boundaries with M_2 barotropic velocities taken from the TPXO7.2 inverse model global solution (Egbert and Erofeeva, 2002, http://volkov.oce.orst.edu/tides/). A Flather boundary condition (Flather, 1976) is applied so that barotropic energy is transmitted out of the domain. Baroclinic (internal) energy is absorbed at the boundaries using the relaxation scheme described by Carter and Merrifield (2007). Both schemes work to stop wave reflection back into the model domain. The boundary forcing is ramped up over the first two tidal cycles of the simulation.

2.1. Model diagnostics

M_2 vertical isopycnal displacement amplitude (ξ_A) and phase (ξ_ϕ) are inferred from the harmonic analyses output and used to verify the numerical model against an observational hydrographic dataset (Section 3).

Baroclinic M_2 energy flux is calculated as

$$\mathbf{F} = \langle \mathbf{u}' p' \rangle \,, \tag{1}$$

where $\mathbf{u}'$ is the baroclinic velocity perturbation, p' is the pressure perturbation, and $\langle \cdot \rangle$ denotes an average over a tidal cycle (e.g., Kunze et al., 2002; Nash et al., 2005). The perturbations $\mathbf{u}'$ and p' are reconstructed from the harmonic constants.

Barotropic-to-baroclinic M_2 energy conversion is calculated as

$$E_{conv} = \langle p'\,(-H)\, w_{bt} \rangle, \tag{2}$$

where $p'(-H)$ is the pressure perturbation at the bottom and $w_{bt} = -\overline{\mathbf{u}} \cdot \nabla H$ is the barotropic vertical velocity (Niwa and Hibiya, 2001). The barotropic velocity perturbation, $\overline{\mathbf{u}}$, is reconstructed from the harmonic constants. Positive values of E_{conv} indicate the transfer of energy from the barotropic tide to the baroclinic tide, whilst negative values are a measure of energy transfer due to the pressure work done on the barotropic tide by the baroclinic tide (Zilberman et al., 2009).

Baroclinic M_2 horizontal kinetic energy (HKE) density is calculated as

$$\mathrm{HKE} = \frac{1}{4}\rho(u_A^2 + v_A^2), \tag{3}$$

where u_A and v_A are perpendicular baroclinic velocity amplitudes and $\rho = 1025$ kg m^{-3} is a reference density. Baroclinic M_2 available potential energy (APE) density is approximated using linear theory as

$$\mathrm{APE} = \frac{1}{4}\rho N^2 \xi_A^2, \tag{4}$$

where ξ_A is the vertical isopycnal displacement amplitude and N is the buoyancy frequency (Kang and Fringer, 2010). For linear freely-propagating progressive internal waves with $\omega \ll N$, the theoretical HKE/APE ratio is

$$\frac{\mathrm{HKE}}{\mathrm{APE}} = \frac{\omega^2 + f^2}{\omega^2 - f^2}, \tag{5}$$

ACCEPTED MANUSCRIPT

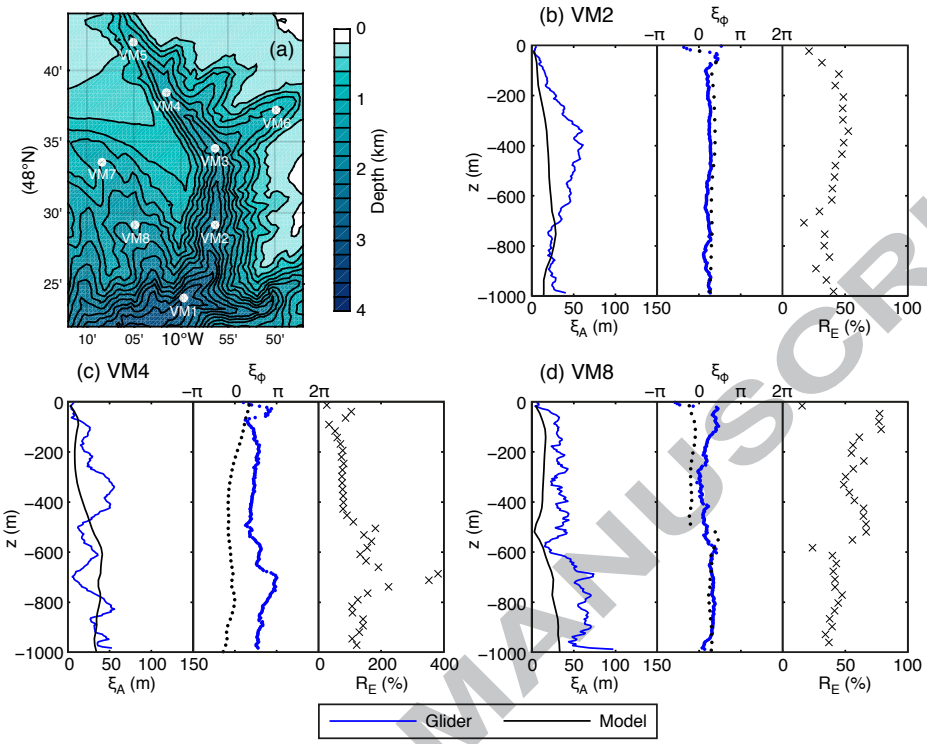

Figure 2: (a) Location of the ocean glider virtual mooring (VM) stations in the eastern limb (Limb 4) of Whittard Canyon. (b) Comparison between observed and modelled M_2 vertical isopycnal displacement amplitude (left panel) and phase (middle panel) for VM2. The right panel is relative error in isopycnal displacement. (c) As (b) but for VM4. (d) As (b) but for VM8.

where ω is the angular frequency of the internal wave and f is the inertial frequency (Gill, 1982). For M_2 internal tides ($\omega = 1.405 \times 10^{-4}$ s^{-1}) at a latitude representative of the study region (48°N), the theoretical HKE/APE ratio is 3.99.

The reflective behaviour of normally incident internal waves approaching a sloping boundary from offshore can be predicted from the ratio of the topographic slope to the internal wave characteristic slope,

$$\alpha = \frac{\partial H / \partial \widetilde{x}}{\left[\left(\omega^2 - f^2\right) / \left(N^2 - \omega^2\right)\right]^{1/2}}, \tag{6}$$

where H is total depth and $\widetilde{x}$ is across-slope distance. If $\alpha < 1$ (subcritical) waves will be transmitted up the slope. If $\alpha > 1$ (supercritical) waves will be reflected back offshore. If $\alpha \simeq 1$ (near-critical) linear theory breaks down, leading to nonlinear effects, wave breaking, and turbulent mixing (Eriksen, 1982). Near-critical values are defined as $0.8 < \alpha < 1.3$ following the experimental results of McPhee-Shaw and Kunze (2002).

3. Model verification

Model skill is assessed through comparison with a hydrographic dataset from the eastern limb (Limb 4) of Whittard Canyon collected by an autonomous ocean glider. The dataset, described in full by Hall et al. (2017), comprises of 8 approximately 36-h tide-resolving virtual mooring[2] (VM) stations, collected between

[2]A glider operating as a virtual mooring repeatedly dives at the same location – collecting a timeseries dataset similar to that from a fixed hydrographic mooring.

ACCEPTED MANUSCRIPT

Table 1: Location of the ocean glider virtual moorings stations, maximum depth of the glider observations at each station, and depth-mean absolute error ($\overline{E}$) and relative error ($\overline{R_E}$) in M_2 vertical isopycnal displacement.

Station	Latitude	Longitude	Depth (m)	$\overline{E}$ (m)	$\overline{R_E}$ (%)
VM1	48°24.0' N	09°59.7' W	975	10.5	165.6
VM2	48°29.1' N	09°59.7' W	980	13.7	38.7
VM3a	48°34.5' N	09°56.4' W	990	16.0	73.8
VM3b	48°34.5' N	09°56.4' W	965	13.7	54.4
VM4	48°38.4' N	10°01.5' W	975	32.0	122.6
VM5	48°42.3' N	10°05.4' W	820	31.1	92.6
VM6a	48°37.2' N	09°49.8' W	980	38.9	85.3
VM6b	48°37.2' N	09°49.8' W	945	16.5	65.1
VM7	48°33.6' N	10°08.4' W	990	31.7	70.8
VM8	48°29.1' N	10°04.8' W	980	20.5	51.1

15th August and 6th September 2015 using an iRobot 1KA Seaglider (SG537; Eriksen et al., 2001). Two stations (VM3 and VM6) were occupied twice, approximately at spring and neap tide. The locations of the VM stations are shown in Figure 2a and detailed in Table 1. Profiles of M_2 vertical isopycnal displacement amplitude and phase were calculated for each station occupation down to nearly 1000 m (820 m for VM5). The station timeseries were too short to separately resolve the S_2 internal tide, so the spring-neap cycle was removed using the TPXO European Shelf solution (Egbert and Erofeeva, 2002; Egbert et al., 2010) by assuming a local internal tide generation site and therefore that the internal spring-neap cycle was phase-locked and proportional to the surface spring-neap cycle.

Comparisons between observed and modelled M_2 displacement amplitude and phase are shown in Figure 2 for three of the 10 station occupations. For all station occupations, modelled displacement amplitude contains less vertical structure than observed and at some stations the model consistently underestimates amplitude (e.g., VM8, Fig. 2d). The relationship between observed and modelled displacement phase is variable; at some stations the phase profiles are almost identical (e.g., VM2, Fig. 2b), at other stations there is noticeable phase offset (e.g., VM4, Fig 2c), while at others observed and modelled phase have different vertical structures.

To quantify the absolute error (E), the root mean square (rms) difference between observed and modelled M_2 displacement over a tidal cycle is calculated following Cummins and Oey (1997), Carter et al. (2008) and Hall et al. (2011). Relative error (R_E) is absolute error divided by observed displacement amplitude and stated as a percentage. Depth-average absolute error ($\overline{E}$) and depth-average relative error ($\overline{R_E}$) are calculated for each station occupation and shown in Table 1. $\overline{E}$ ranges from 10.5 m to 38.9 m, with the largest errors occurring where there are large phase offsets. $\overline{R_E}$ ranges from 38.7% to 165.6%, comparable to a previous application of POM to Monterey Canyon (30-209%; Carter, 2010). A component of this error might be due to insufficient resolution of the complex canyon bathymetry; Whittard Canyon features steep walls (even vertical and overhanging) that cannot be adequately resolved by 500-m model bathymetry. Zilberman et al. (2009) showed that the generation of higher internal wave modes in POM simulations is limited by bathymetric resolution, which may explain the underestimate of vertical structure in the model output. Furthermore, the morphology of Whittard Canyon is likely to be constantly evolving due to erosional and depositional processes (Amaro et al., 2015).

4. Results

4.1. Internal tide generation sites

The sloping bathymetry of Whittard Canyon and the surrounding region provide many potential internal tide generation sites through scattering of the barotropic tide (Bell, 1975; Baines, 1982). As shown by

ACCEPTED MANUSCRIPT

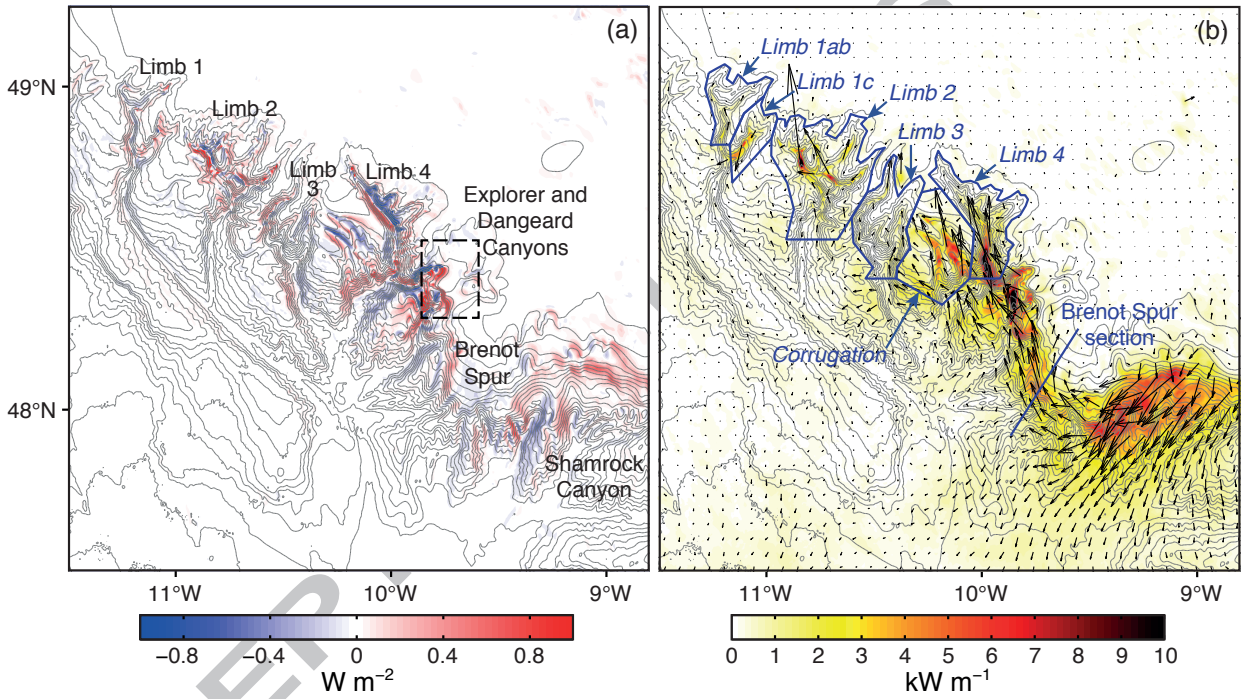

Figure 3: (a) Barotropic-to-baroclinic M_2 energy conversion in the Whittard Canyon region. Positive values indicate sources of baroclinic energy. (b) Depth-integrated baroclinic M_2 energy flux. Vectors are plotted every 10 grid points (5 km) in each direction. The underlying colour is the energy flux magnitude. The bathymetric contour interval is 200 m. The six areas that energy budgets are calculated for are shown in blue, along with the Brenot Spur section.

ACCEPTED MANUSCRIPT

Rainville et al. (2010), internal tides radiating from multiple generation sites form complex patterns of constructive and destructive interference and make it difficult to diagnose the exact source of any particular beam. However, realistic interpretation of internal tide generation sites in the Whittard Canyon region can be made by comparing barotropic-to-baroclinic M_2 energy conversion (Fig. 3a) with depth-integrated baroclinic M_2 energy flux (Fig. 3b).

Much of the baroclinic energy entering Whittard Canyon originates to the southeast, along the Celtic Sea shelf break, where baroclinic energy fluxes are consistent with areas of high (>0.2 W m^{-2}) barotropic-to-baroclinic energy conversion. Internal tide generation in this region can be roughly divided into two areas: the upper reaches of Shamrock Canyon, to the east of Brenot Spur, and the western flank of Brenot Spur, which is incised by Explorer and Dangeard Canyons (as described by Stewart et al., 2014). Two beams of baroclinic energy radiate from these generation sites: a strong, narrow beam propagates northwest, around Brenot Spur, and into Limb 4, whilst a second strong, wider beam propagates southwest from Shamrock Canyon over the abyssal plain. The northwest propagating beam is constrained by the bathymetry of Limb 4 with large depth-integrated baroclinic energy fluxes (>8 kW m^{-1}) directed up-canyon in its upper reaches. Baroclinic energy fluxes throughout the rest of the Whittard Canyon system are much lower in comparison to those in Limb 4, indicating either a lesser, or completely absent, influence of the generation sites to the southeast.

Internal tide generation also occurs within the canyon itself and is identifiable by areas of positive barotropic-to-baroclinic energy conversion consistent with up- or down-canyon depth-integrated baroclinic energy fluxes (for example, Limb 1b, Limb 2a, and the lower reaches of Limb 4a). In the upper reaches of Limb 2a and Limb 4a, adjacent areas of positive (>0.8 W m^{-2}) and negative (<−0.8 W m^{-2}) energy conversion imply that local internal tide generation is in part balanced by baroclinic energy loss to the barotropic tide. Negative energy conversion occurs when the pressure perturbation from remotely generated internal tides is larger than, and out of phase with, the pressure perturbation from local barotropic forcing (e.g., Zilberman et al., 2009; Kelly and Nash, 2010). The presence of areas of negative energy conversion indicates that there are multiple generation sites of importance to the internal tide field within the canyon. Adjacent areas of positive and negative energy conversion also occur in Limb 1a and Limb 3a, but the magnitude of energy conversion is lower (>0.4 W m^{-2} and <−0.4 W m^{-2}). The spatial distribution of energy conversion is fairly consistent throughout the canyon, with positive conversion tending to occur on the western walls of the canyon limbs and negative conversion tending to occur on the eastern walls.

These result compare favourably with a fine-resolution (115-m) nonhydrostatic model simulation of the internal tide field over the Celtic Sea continental shelf and shelf break by Vlasenko et al. (2014). Their simulation shows packets of internal solitary waves, superposed on semidiurnal internal tides, radiating from several local generators: the shelf break east of the eastern limb of Whittard Canyon; Petite Sole Canyon; and Brenot Spur. These three areas are also apparent internal tide generation sites in the high-resolution (500-m) hydrostatic model simulation presented here.

4.2. Internal tide propagation through Whittard Canyon

Depth-integrated baroclinic M_2 energy fluxes in the Limb 4 of Whittard Canyon exceed 8 kW m^{-1}, comparable to energy fluxes observed in tidally energetic submarine canyons such as Monterey (up to 5 kW m^{-1}; Kunze et al., 2002; Zhao et al., 2012; Wain et al., 2013), Eel (7.6 kW m^{-1}; Waterhouse et al., 2017) and Gaoping (14 kW m^{-1}; Lee et al., 2009). In the upper reaches of Whittard Canyon, depth-integrated baroclinic energy flux is primarily directed up-canyon, suggesting topographic steering of the internal tide. However, there are locations where depth-integrated energy flux is directed down-canyon, for example in Limbs 1b and 2c.

To better diagnose topographic steering of the internal tide by the steep canyon walls, near-bottom baroclinic M_2 tidal current ellipses along the canyon thalwegs are shown in Figure 4. In the lower reaches of all four major canyon limbs, velocities are low (<0.1 m s^{-1}) and the current ellipses almost circular. Moving up-canyon, the ellipses become more rectilinear (i.e., the semi-minor axis is small compared to the semi-major axis), with the semi-major axes orientated along the canyon thalwegs. In the upper reaches of the canyon, along-thalweg velocities are up to 0.4 m s^{-1}. These results are in general agreement with near-bottom current velocity observations within the canyon. The deepest measurements (>4000 m; van Weering

ACCEPTED MANUSCRIPT

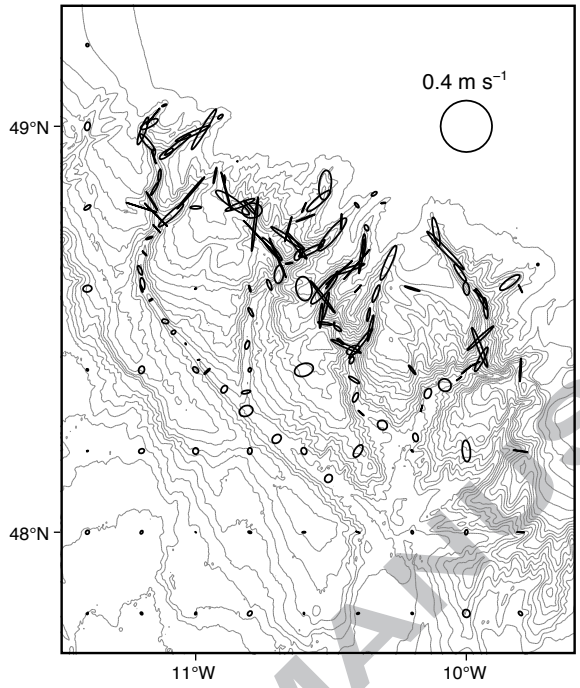

Figure 4: Near-bottom baroclinic M_2 tidal current ellipses in Whittard Canyon. Current ellipses shallower than 300 m are omitted for clarity.

et al., 2000; Amaro et al., 2015) contain weak semidiurnal signals with velocities $\leq$0.1 m s^{-1}. Measurements farther up-canyon feature increasingly energetic near-bottom currents, for example, 0.16 m s^{-1} at 3752 m (Reid and Hamilton, 1990) and 0.24-0.40 m s^{-1} at 1000 m (Duros et al., 2011).

4.3. Kinetic and potential energy

Depth-integrated baroclinic M_2 HKE within the canyon is maximum ($\sim$10 kJ m^{-2}) in Limbs 1b, 2a and 4a (Fig. 5a) and closely matches the spatial distribution of depth-integrated baroclinic energy flux (Fig. 3b). HKE is also elevated to the east of Brenot Spur, identified as a key internal tide generation site. Depth-integrated baroclinic M_2 APE is elevated over a larger proportion of the canyon than HKE, reaching a maximum (>12 kJ m^{-2}) in Limbs 1b, 2a, 2b and 4a and also to the east of Brenot Spur (Fig. 5b).

Away from the canyon bathymetry, APE is typically lower than HKE, indicating a background HKE/APE ratio greater than one. This is expected as the theoretical value for a progressive M_2 internal tide in this region is 3.99. However, when averaged over the area of individual canyon limbs (defined in Section 5), HKE/APE is less than one (Table 2). This discrepancy has previously been identified Monterey Canyon and it was hypothesised by Petruncio et al. (1998) that reduced HKE was a consequence of across-canyon motion being constrained by the narrow bathymetry. The complex, dendritic morphology of Whittard Canyon could potentially have a similar effect. An alternatively explanation was provided by Kunze et al. (2002), who argued that excess APE in Monterey Canyon was the result of additional vertical isopycnal displacement caused by local barotropic tidal flow over the sloping bathymetry. Following Kunze et al. (2002), Hall and Carter (2011) removed this barotropic contribution to vertical isopycnal displacement during analysis of their POM simulation of Monterey Canyon and it increased HKE/APE towards to the theoretical value. Applying the same method to Whittard Canyon, we find that that HKE/APE is increased to greater than one when averaged over individual canyon limbs, although in five of the six areas it remains <50% of the theoretical value.

ACCEPTED MANUSCRIPT

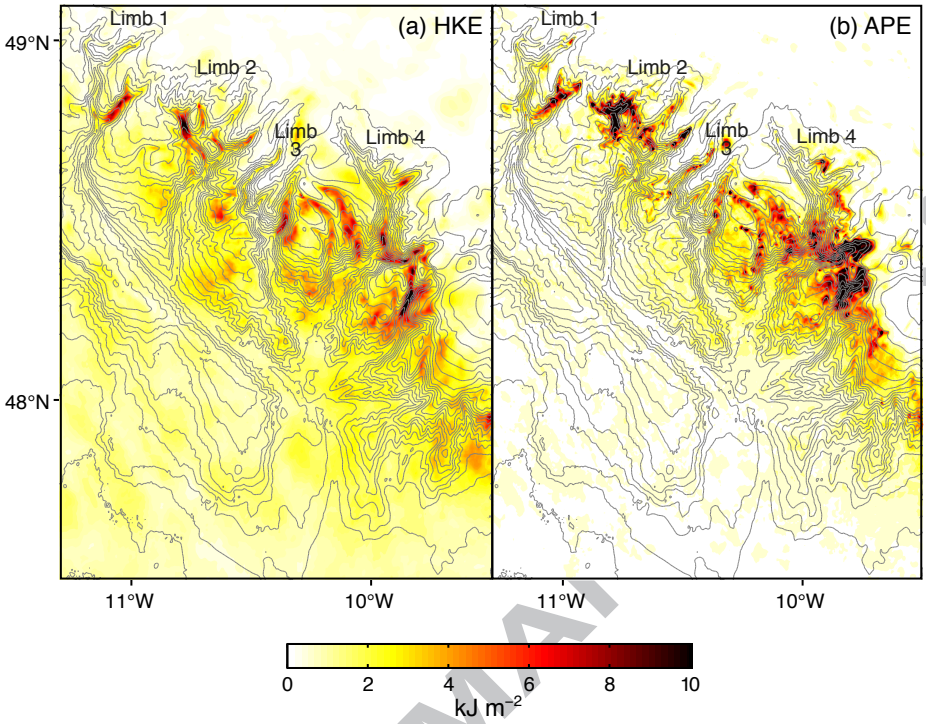

Figure 5: (a) Depth-integrated baroclinic M_2 HKE in Whittard Canyon. (b) Depth-integrated baroclinic M_2 APE.

A third explanation for the low HKE/APE ratio is that the internal tides within the canyon exist as standing or partly standing waves. Standing waves (the superposition of two progressive waves with the same frequency and amplitude, but propagating in opposite directions) result in an oscillation of HKE/APE between zero and infinity over consecutive half horizontal wavelengths (Martini et al., 2007). Partly standing waves, where the two component waves have different amplitudes, result in a lesser oscillation of HKE/APE, but nevertheless, it deviates from the theoretical value for a fully progressive internal wave. Hall et al. (2017) suggest that the M_2 internal tide in Limb 4 of Whittard Canyon is a partly standing wave with HKE/APE varying between 1 and 4.5. The down-canyon component wave is thought to be a reflection of the up-canyon component wave from steep, supercritical bathymetry near the head of the canyon limb.

4.4. Depth-structure of the internal tide

The depth-structure of the internal tide within Whittard Canyon is presented as along-thalweg sections[3] for the two most tidally energetic canyon limbs: Limb 2a (Fig 6) and Limb 4a (Fig. 7). There is no noticeable across-canyon asymmetry in internal tide energetics so across-canyon sections are not shown. In both canyon limbs, along-canyon baroclinic M_2 energy flux is bottom intensified over the depth range 500-2500 m, suggesting topographic focusing of the internal tide (e.g., Gordon and Marshall, 1976; Hotchkiss and Wunsch, 1982). In both limbs, the up-canyon near-bottom energy flux is accompanied by an up-canyon energy flux near the surface with near-zero energy flux (or low-magnitude down-canyon energy flux) at mid-depth; this is the expected structure for a dominant mode-1 internal tide. Down-canyon energy fluxes are most prevalent in the lower reaches of the canyon where topographic focusing has less influence. Across-canyon energy flux is dominated by small-scale variability that is primarily attributed to the meandering path of the thalweg rather than variation in the direction of the energy flux (see Hall et al., 2014). Bottom intensification of baroclinic M_2 HKE and APE is consistent with along-canyon energy flux intensification.

[3]Along-thalweg distance is defined as positive up-canyon and zero at $H = 1000$ m.

ACCEPTED MANUSCRIPT

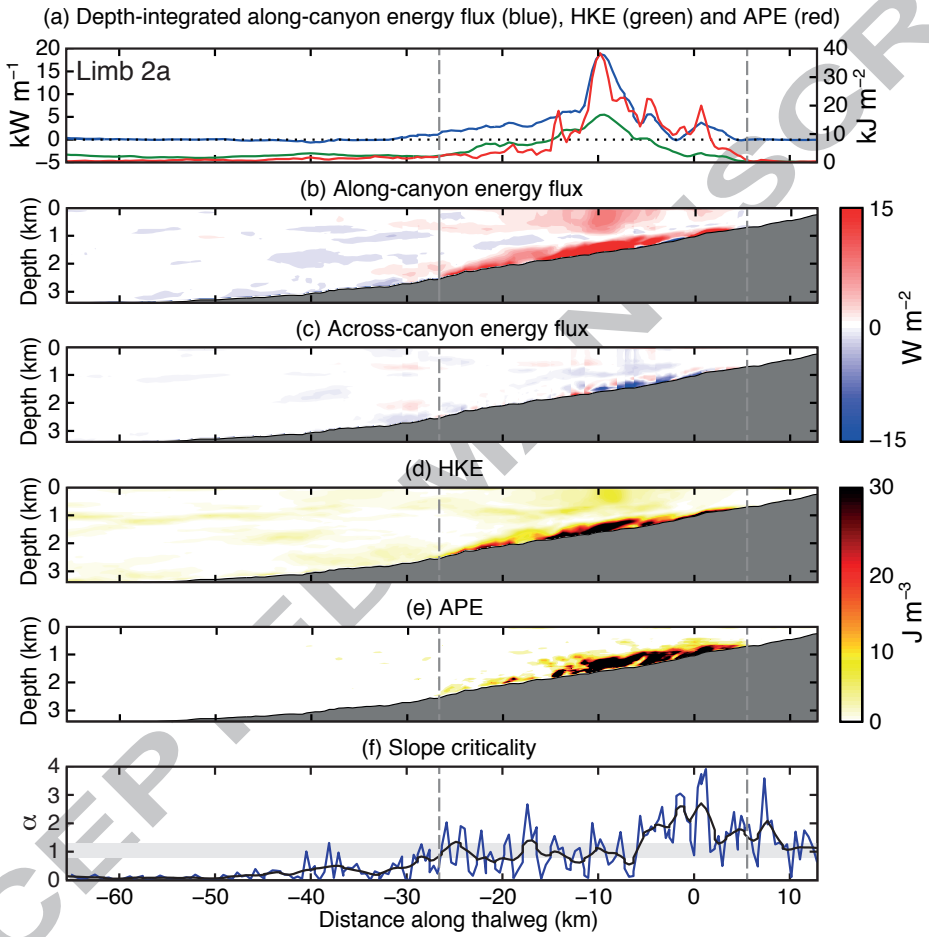

Figure 6: Along-thalweg section for Limb 2a of Whittard Canyon. (a) Depth-integrated along-canyon baroclinic M_2 energy flux (blue), HKE (green), and APE (red) with distance along the thalweg. (b) Along-canyon and (c) across-canyon baroclinic M_2 energy flux with distance along the thalweg. Positive along-canyon values are toward the head of the canyon limb. Positive across-canyon values are to the left when looking up canyon. (d) Baroclinic M_2 HKE and (e) APE with distance along the thalweg. (f) Along-thalweg slope criticality to the M_2 internal tide (blue) and smoothed using a 5-km running mean (black). Near-critical values ($0.8 < \alpha < 1.3$; McPhee-Shaw and Kunze, 2002) are indicated in grey. The dashed grey lines indicate the distance over which bottom intensification occurs.

ACCEPTED MANUSCRIPT

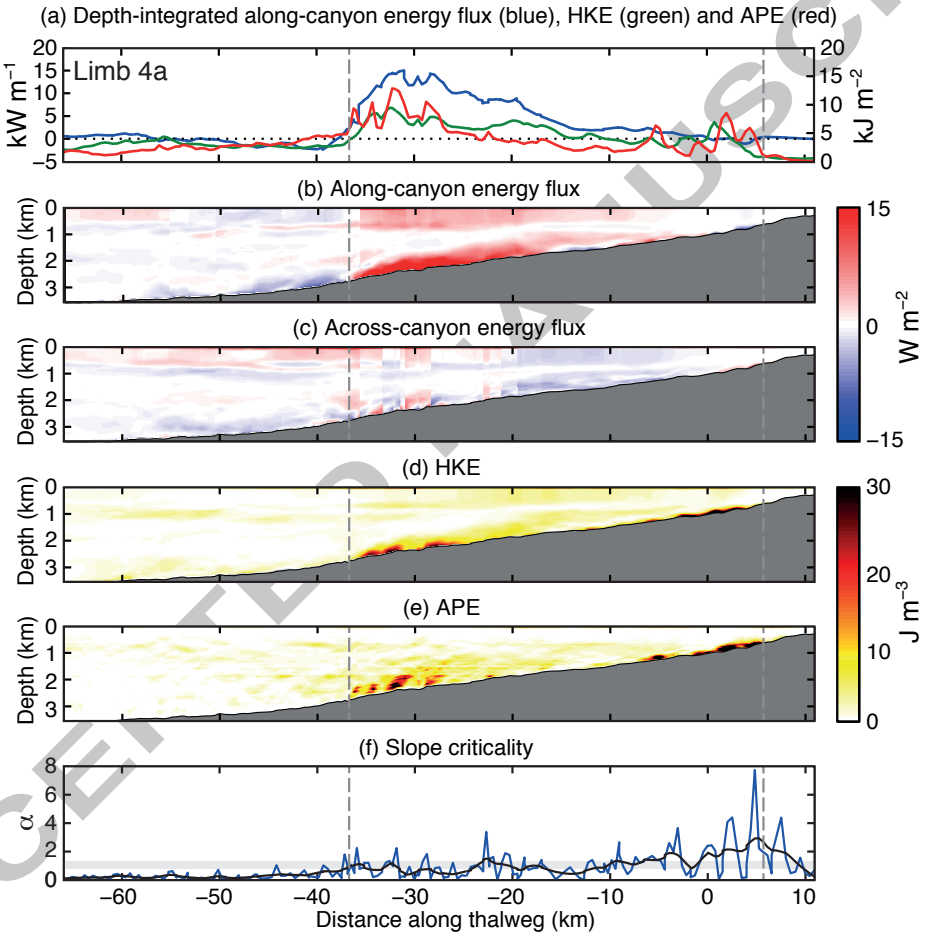

Figure 7: As Figure 6 but for Limb 4a of Whittard Canyon.

ACCEPTED MANUSCRIPT

Table 2: Barotropic-to-baroclinic M_2 energy conversion (E_{conv}) integrated over the six areas shown in Figure 3b. Net energy conversion is split into positive and negative components. Baroclinic M_2 energy flux divergence (∇F) for the same six areas. Total baroclinic energy dissipation in the six areas and dissipation rate per kilogram of seawater. HKE/APE ratio for the six areas. Values in brackets have had the barotropic contribution to vertical isopycnal displacement removed.

Area	Area-integrated E_{conv}			∇F	Energy dissipation		HKE/APE
	Net (MW)	Pos. (MW)	Neg. (MW)	(MW)	Total (MW)	Rate ($\times 10^{-8}$ W kg^{-1})	
Limb 1ab	7.9	15.9	−8.0	−1.8	9.7	3.79	0.66 (1.44)
Limb 1c	12.5	15.5	−3.0	7.7	4.8	2.10	0.73 (1.83)
Limb 2	70.3	101.7	−31.3	2.9	67.4	5.20	0.63 (1.44)
Limb 3	16.8	32.6	−15.9	−2.9	19.7	2.65	0.81 (1.99)
Corrugation	36.9	65.8	−28.9	−35.2	72.1	7.65	0.87 (2.16)
Limb 4	21.3	81.6	−60.4	−15.4	36.7	6.37	0.66 (1.51)

When depth-integrated, along-canyon energy flux, HKE and APE are all elevated over the distance of bottom intensification. Assuming the internal tide is propagating up-canyon, we calculate α along the limb thalwegs and find that the down canyon extent of bottom intensification closely corresponds to the point that along-thalweg slope becomes near-critical to the M_2 internal tide. This is expected as baroclinic energy is trapped against the boundary during critical reflection (Cacchione and Wunsch, 1974). The up canyon extent of bottom intensification is less well defined, but in both cases occurs where along-thalweg slope is supercritical. Supercritical bathymetry near the heads of the canyon limbs provides a mechanism for the formation of standing or partly standing internal tides within the canyon.

5. Canyon energy budget

As discussed previously, different patterns of barotropic-to-baroclinic energy conversion and baroclinic energy flux occur in the multiple limbs of Whittard Canyon. To investigate these differences in more detail, and to estimate baroclinic energy dissipation within the canyon, the upper reaches of the canyon is divided into six areas: five areas cover individual or groups of canyon limbs, the sixth covers the corrugated area of shelf slope between Limbs 3b and 4a (Fig. 3b). Each area is defined using the canyon bathymetry and spatial pattern of depth-integrated baroclinic energy flux as a guide; the 300-m isobath is used to define the northernmost extent of each area. Area-integrated barotropic-to-baroclinic energy conversion and baroclinic energy flux divergence (net energy flux out of the area) are calculated for each area[4] (Table 2). The residual is assumed to be the total baroclinic energy dissipation in the area.

All six areas within Whittard Canyon feature positive net energy conversion, with the largest value occurring in *Limb 2* (70.3 MW). Positive energy conversion implies local internal tide generation whilst negative values indicate work done on the barotropic tide by the baroclinic tide (Zilberman et al., 2009), therefore it is instructive to also look at the positive and negative components of energy conversion. The largest value of positive energy conversion also occurs in *Limb 2* (101.7 MW), although both *Limb 4* and the *Corrugation* area also have large positive conversion values (81.6 MW and 65.8 MW, respectively). In each area, local internal tide generation, associated with positive conversion, is partially compensated by negative conversion, although the degree to which this occurs varies. For example, 74% of positive conversion is compensated for by negative conversion within *Limb 4* whilst in *Limb 1c* only 19% is compensated for.

As anticipated from the cessation of the northwest propagating beam of depth-integrated baroclinic energy flux (Fig. 3b), baroclinic energy flux divergence is strongly negative (convergent) in *Limb 4* and the *Corrugation* area (−15.4 MW and −35.2 MW, respectively). The positive energy flux divergence in *Limb 1c*

[4]The names of the energy budget area are italicised to avoid confusion with names of the canyon limb thalwegs.

ACCEPTED MANUSCRIPT

Table 3: Energy budgets for four model simulations with decreasing bathymetric resolution: barotropic-to-baroclinic M_2 energy conversion (E_{conv}) integrated over the whole model domain and the area of the Whittard Canyon system (Fig. 8a, dashed black box); baroclinic M_2 energy flux divergence (∇F) for the model domain and the canyon area; and total baroclinic energy dissipation in the model domain and the canyon area. The *0.5 km* simulation is in bold because this is the control simulation.

Model simulation	Area-integrated E_{conv}		∇F		Total energy dissipation	
	Domain (GW)	Canyon (GW)	Domain (GW)	Canyon (GW)	Domain (GW)	Canyon (GW)
0.5 km	**0.66**	**0.32**	**0.14**	**−0.05**	**0.52**	**0.37**
1.5 km	0.63	0.31	0.12	−0.06	0.51	0.37
5.5 km	0.54	0.26	0.13	−0.07	0.41	0.33
15 km	0.37	0.16	0.10	−0.06	0.27	0.22

corresponds to the down-canyon depth-integrated energy fluxes seen in Figure 3b, indicating that baroclinic energy is leaving Limb 1c and entering Limb 1a. Positive energy flux divergence also occurs in *Limb 2*.

Total baroclinic energy dissipation in the upper reaches of the canyon (sum of all six areas) is 210 MW. Net energy conversion in the upper reaches is 167 MW, so considering the upper canyon as a whole, the majority of baroclinic energy dissipated is locally converted. To quantify the amount of baroclinic energy that enters the Whittard Canyon system from generation sites to the southeast, total baroclinic energy flux around Brenot Spur is calculated. Along-slope energy flux, integrated across the Brenot Spur section, (Fig. 3b) is 44 MW, which can account for the majority of the remaining baroclinic energy dissipation in the upper reaches of the canyon.

Considering the canyon limbs separately, total baroclinic energy dissipation is largest in the *Corrugation* area (72.1 MW) and *Limb 2* (67.4 MW). However, for direct comparison it is important to take into account the size of each area. An average dissipation rate can be calculated by dividing total baroclinic energy dissipation by the mass of seawater in each area (area × average-depth × seawater density). The dissipation rate is highest in the *Corrugation* area (7.65×10^{-8} W kg^{-1}) and *Limb 4* (6.37×10^{-8} W kg^{-1}), further evidence that these areas are important sinks of the baroclinic energy entering the canyon from the generation sites to the southeast. It is interesting to note that baroclinic energy dissipation is high in both *Limb 2* and *Limb 4*, but for different reasons: the baroclinic energy dissipated in *Limb 2* is primarily the result local internal tide generation (large positive net energy conversion) whilst in *Limb 4* negative energy flux divergence contributes nearly as much to baroclinic energy dissipation as positive net energy conversion. Dissipation rates in the other limbs (*Limb 1ab*, *Limb 1c* and *Limb 3*) are small as a result of both low energy flux divergence and low net energy conversion.

The dissipation rates in the *Corrugation* area and *Limb 4* are smaller than those inferred by Hall et al. (2017) in roughly the same areas; 3.6×10^{-7} W kg^{-1} and 1-2.5 $\times 10^{-7}$ W kg^{-1}, respectively. However, considering the limitations of the glider observations and the assumptions made in that study to infer energy flux divergence (assumed equal to total energy dissipation), a factor of 2-4 difference is acceptable. Previous POM simulations suggest that dissipation rates in Monterey and Ascension Canyons are 4-8 $\times 10^{-8}$ W kg^{-1} (Gregg et al., 2011), close to the range of values calculated here. However, turbulent kinetic energy dissipation rates in submarine canyons worldwide, determined from microstructure profiler measurements or Thorpe scale analysis of CTD data, range over several orders of magnitude (e.g., Lueck and Osborn, 1985; Carter and Gregg, 2002; Gregg et al., 2005; Lee et al., 2009; Kunze et al., 2012; Waterhouse et al., 2017). To fully investigate turbulent mixing processes in Whittard Canyon will require a comprehensive survey using a microstructure profiler or a microstructure sensor equipped glider.

6. Bathymetric resolution

The model simulation described above uses 500-m resolution bathymetry, the highest resolution freely available that covers the majority of the Whittard Canyon region. Given that the model domain needs to

ACCEPTED MANUSCRIPT

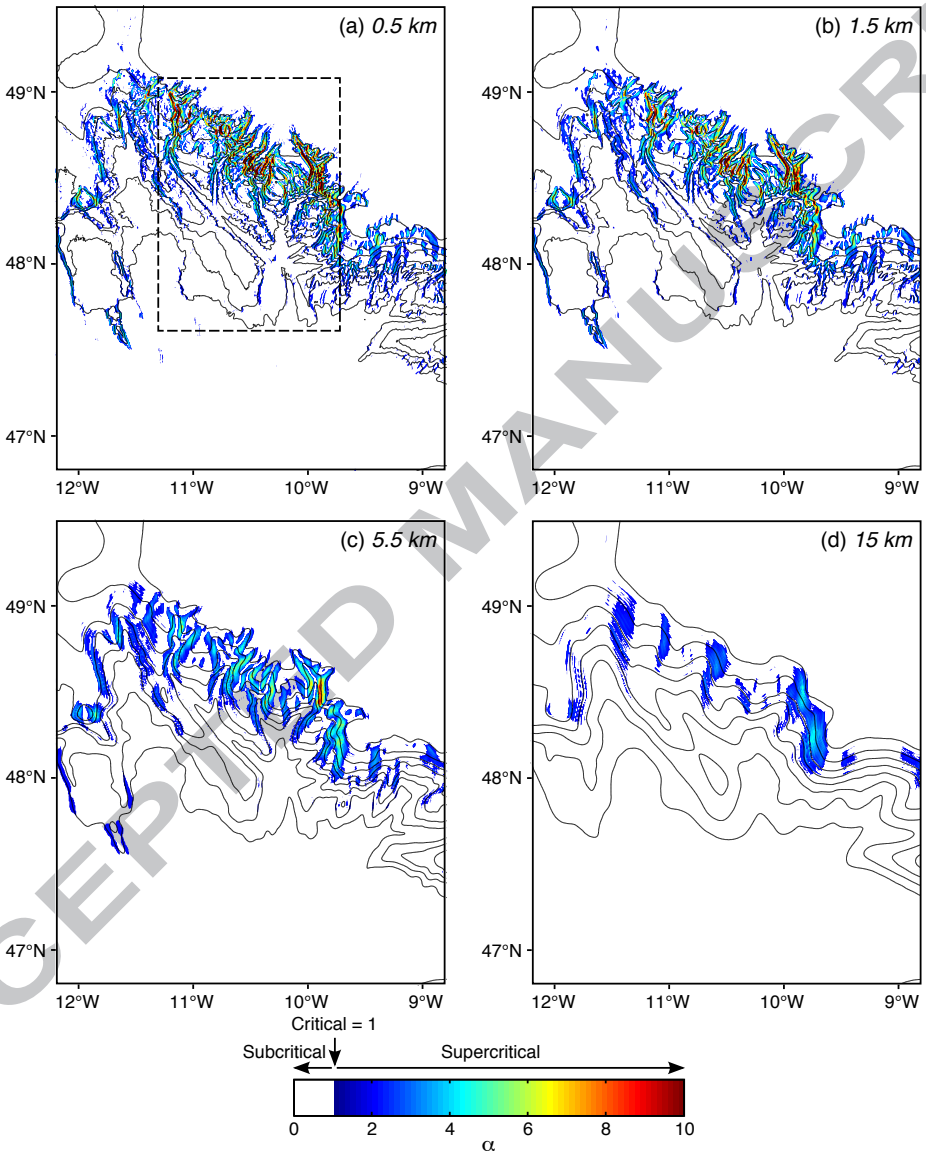

Figure 8: Maximum slope criticality to the M_2 internal tide in the Whittard Canyon region for four model simulations with decreasing bathymetric resolution: (a) *0.5 km*, (b) *1.5 km*, (c) *5.5 km*, and (d) *15 km*.

ACCEPTED MANUSCRIPT

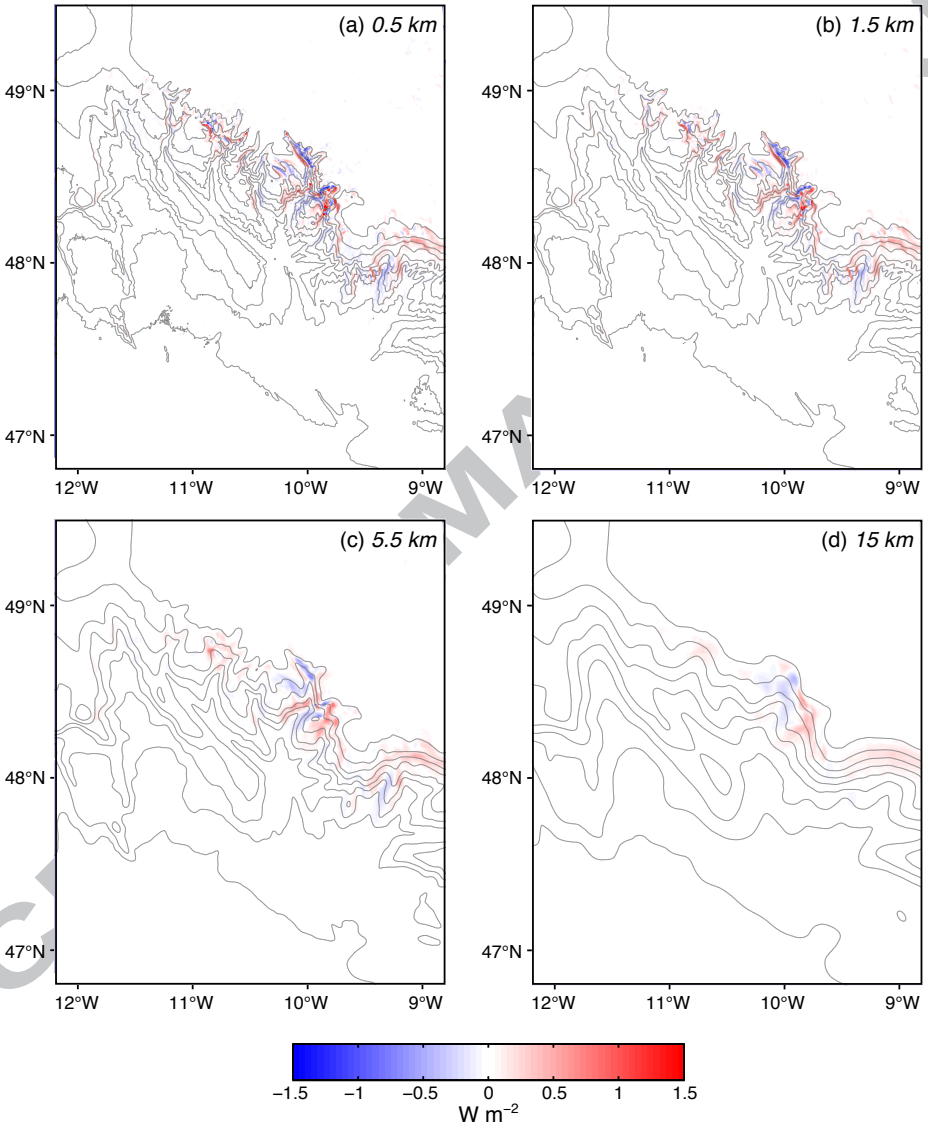

Figure 9: Barotropic-to-baroclinic M_2 energy conversion in the Whittard Canyon region for four model simulations with decreasing bathymetric resolution: (a) *0.5 km*, (b) *1.5 km*, (c) *5.5 km*, and (d) *15 km*.

ACCEPTED MANUSCRIPT

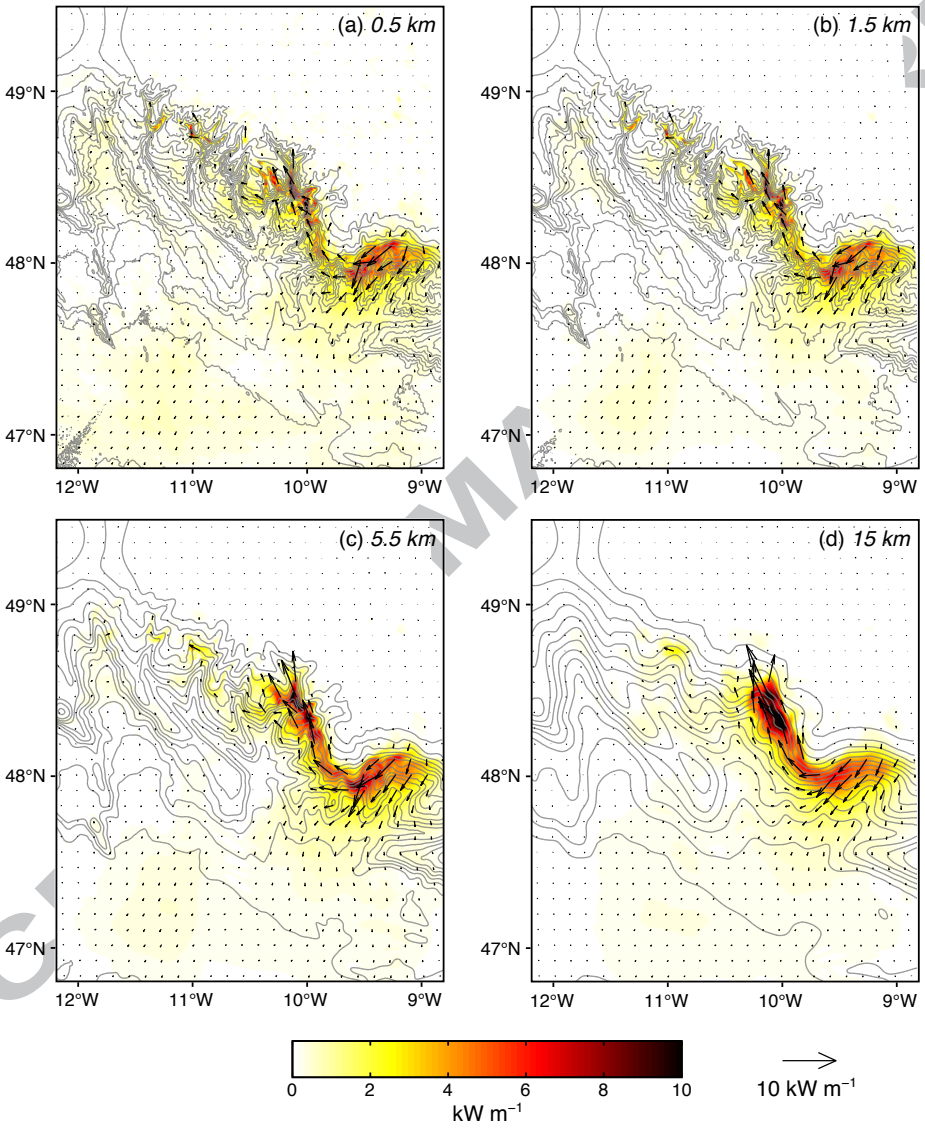

Figure 10: Depth-integrated baroclinic M_2 energy flux in the Whittard Canyon region for four model simulations with decreasing bathymetric resolution: (a) *0.5 km*, (b) *1.5 km*, (c) *5.5 km*, and (d) *15 km*. Vectors are plotted every 20 grid points (10 km) in each direction. The underlying colour is the energy flux magnitude.

ACCEPTED MANUSCRIPT

be large enough to include all likely internal tide generation sites, resolution is also limited by computational expense. Previous work by Zilberman et al. (2009) showed the importance of using high-resolution bathymetry to simulate internal tide generation at the Mid-Atlantic Ridge. Here we investigate the sensitivity of barotropic-to-baroclinic energy conversion and baroclinic energy flux to bathymetric resolution for Whittard Canyon and the surrounding region.

Three simplified bathymetric grids are created by smoothing the original 500-m resolution bathymetry using 3×3-point (*1.5 km*), 11×11-point (*5.5 km*), and 30×30-point (*15 km*) square window mean filters. Three sensitivity simulations are then run using the simplified bathymetric grids with identical initial conditions and boundary forcing to the control simulation (*0.5 km*). Model resolution remains 500-m in the horizontal. The *1.5 km* grid retains the main bathymetric features of the canyon, but with less topographic roughness. The filter used for the *5.5 km* grid is wider than the minor canyon limbs so the resulting bathymetry contains only the major limbs. The filter used for the *15 km* grid effectively removes all of the canyon limbs, leaving a smooth, gently undulating continental slope. The latter case demonstrates how the internal tide field would change in the absence of the Whittard Canyon system.

Smoothing model bathymetry always reduces topographic slope gradient which results in a tendency towards lower values of α. This potentially affects both the modal structure of locally generated internal tides (Garrett and Kunze, 2007) and reflection of remotely generated internal tides (Hall et al., 2013). This tendency towards lower α values is evident in the four bathymetric grids (Fig. 8). With the original 500-m resolution bathymetry, large areas of the upper reaches of Whittard Canyon are supercritical to the M_2 internal tide (primarily due to the steep canyon walls), whereas the abyssal plain, continental shelf, and thalwegs of the lower reaches of the canyon are subcritical. With increased smoothing, the area of the model domain that is subcritical ($\alpha < 0.8$) increases from 85.5% to 94.7%, while the area that is supercritical ($\alpha > 1.3$) decreases from 9.0% to 1.9% and the area that is near-critical ($0.8 < \alpha < 1.3$) decreases from 5.5% to 3.4%. Spatially, the *1.5 km* grid is broadly similar to the *0.5 km* grid. However, substantial difference arise in the *5.5 km* grid; the canyon walls are no longer entirely supercritical and the entire length of the thalwegs, from the canyon mouth to the heads, are subcritical. The *15 km* grid bears little resemblance to the original *0.5 km* grid, however, the area to the west of Brenot Spur remains supercritical.

The spatial pattern of barotropic-to-baroclinic M_2 energy conversion (Fig. 9) and depth-integrated M_2 baroclinic energy flux (Fig. 10) is similar for the *0.5 km* and *1.5 km* model simulations. However, for the *5.5 km* simulation there is notably less variability in energy conversion and fewer areas of intensified energy flux in Limbs 1 and 2. The *15 km* simulation features a pattern of positive energy conversion to the east of Bernot Spur and a combination of positive and negative energy conversion to the west. The energy flux for this simulation is maximum to the west of the spur, where Limb 4 of Whittard Canyon is found in the higher resolution grids. Interestingly, energy flux around Bernot Spur increases with reduced bathymetric resolution.

To quantify these results, barotropic-to-baroclinic energy conversion is integrated over the whole model domain and the area of the Whittard Canyon system (indicated by the dashed black box in Fig. 8a) for each model simulation. Baroclinic energy flux divergence is also calculated for the model domain and canyon area, along with the residual (assumed to be total baroclinic energy dissipation). Domain-integrated energy conversion decreases from 0.66 GW for *0.5 km* to 0.37 GW for *15 km*, almost a 45% reduction. (Table 3). Integrated over the canyon area, energy conversion decreases a proportionally similar amount (50%), from 0.32 GW to 0.16 GW. For all simulations, energy flux divergence is positive for the whole model domain and negative (convergent) for the canyon area, but there is no monotonic change with bathymetric resolution. Energy flux divergence in the canyon only varies between -0.05 GW and -0.07 GW so is always small compared to canyon-integrated energy conversion. Total baroclinic energy dissipation in the model domain decreases with decreasing bathymetric resolution (0.53 GW for *0.5 km* to 0.27 GW for *15 km*), possibly due to reduced topographic scattering to higher internal wave modes. In the canyon area, baroclinic energy dissipation is similar for *0.5 km* and *1.5 km* (0.37 GW) then decreases with decreasing bathymetric resolution to 0.22 GW for *15 km*. These results suggest that at least 1.5-km resolution bathymetry is required to adequately resolve the semidiurnal internal tide field in this region of complex topography.

ACCEPTED MANUSCRIPT

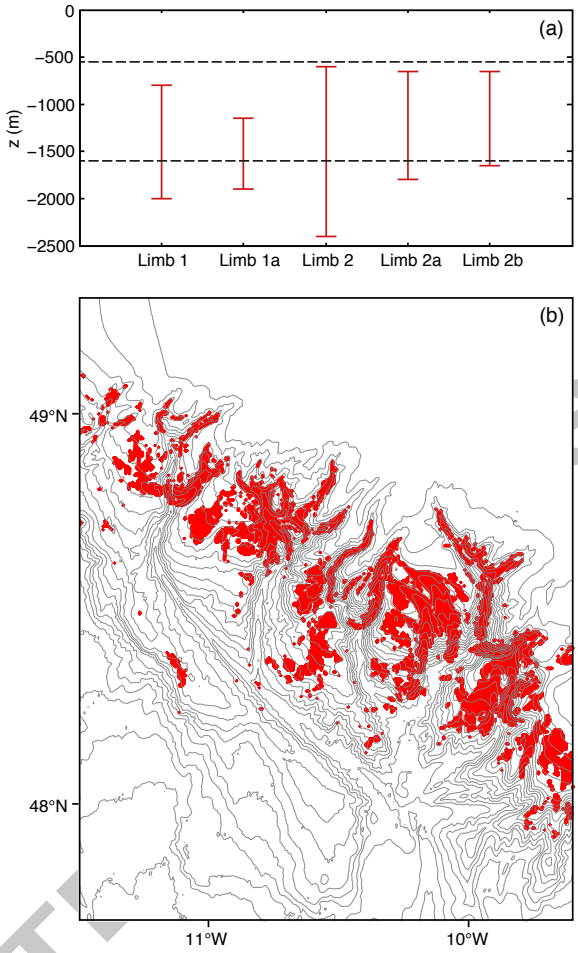

Figure 11: (a) Depth ranges of bottom-intensified along-canyon baroclinic M_2 energy fluxes in the model simulation (red) compared with the depth range observed intermediate nepheloid layers are sourced (dashed black lines; Wilson et al., 2015b) (b) Locations in Whittard Canyon where rms near-bottom baroclinic M_2 tidal current speed exceeds 0.15 m s^{-1}.

7. Discussion: implications for nepheloid layer generation

Several studies have linked shoaling and reflection of internal waves with sediment resuspension and nepheloid layer formation (e.g., Thorpe and White, 1988; McPhee-Shaw and Kunze, 2002; McPhee-Shaw et al., 2004; Bourgault et al., 2014) and specifically focusing of internal wave energy within submarine canyons (e.g., Puig and Palanques, 1998; Puig et al., 2004). Recent work by Huvenne et al. (2011), Johnson et al. (2013) and Wilson et al. (2015b) have mapped both benthic and intermediate nepheloid layers within Whittard Canyon and postulated that internal tides are a major control on their formation. The permanent thermocline (1000-2000 m, Fig. 1c) is thought to act as a waveguide for freely-propagating internal tides, focusing their energy at the seabed (Puig and Palanques, 1998). Once material has been resuspended, the thermocline then acts as an isopycnal surface along which resuspended material can be held in suspension and advected away from the slope. As discussed in Section 4.4, along-canyon baroclinic energy fluxes in some limbs of Whittard Canyon are bottom intensified over the depth range 500-2500 m and there is considerable overlap between the depth ranges that bottom-intensified energy fluxes are simulated and the depth range over which the observed intermediate nepheloid layers are assumed to be sourced (Fig. 11a).

For the North-East Atlantic margin, Thomsen and Gust (2000) suggest current speeds of 0.15 m s^{-1}

ACCEPTED MANUSCRIPT

are required for resuspension of organic material. As shown in Figure 11b, rms near-bottom baroclinic tidal current speed exceeds this threshold value over much of the upper reaches of Whittard Canyon and specifically along the canyon limb thalwegs. The occurrence of nepheloid layers has also been postulated to be driven by anthropogenic causes (Wilson et al., 2015a) and therefore further work must be carried out to separate the internal tide influence from other factors. However, energetic hydrodynamic conditions resulting from internal tide focusing, simulated here in several limbs of Whittard Canyon, are likely to have some effect on sedimentation rates and resuspension of organic material.

8. Summary

A modified version of the Princeton Ocean Model is used to simulate the semidiurnal internal tide within Whittard Canyon, a large, dendritic submarine canyon system that incises the Celtic Sea continental slope. Much of the internal tide energy entering Whittard Canyon originates to the southeast, along the Celtic Sea shelf break. Internal tide generation also occurs within the canyon itself, but is in part compensated by areas of negative energy conversion. The internal tide is topographically steered through the major limbs and along-canyon energy flux is bottom intensified, suggesting topographic focusing. The down canyon extent of bottom intensification closely corresponds to the point that along-canyon slope becomes near-critical to the semidiurnal internal tide. Some of the canyon's limbs are net sources of internal tide energy whilst others are net sinks. Finally, the effect of bathymetric resolution on internal tide generation and propagation is investigated. Decreasing the bathymetric resolution reduces internal tide generation and energy dissipation in both Whittard Canyon and the model domain as a whole. At least 1.5-km resolution bathymetry is required to adequately resolve the semidiurnal internal tide field in this region of complex topography.

Acknowledgments

Tahmeena Aslam was supported by a Centre for Environment Fisheries and Aquaculture Science and University of East Anglia Ph.D. studentship. Seaglider SG537 is owned and maintained by the UEA Marine Support Facility. It was deployed and recovered from the UK Natural Environment Research Council research vessel RRS James Cook (JC125) as part of the CODEMAP project (European Research Council Starting Grant 258482). The CTD cast used to initialise the numerical model was collected from RSS James Cook during an earlier cruise (JC36). Helpful comments on the manuscript were provided by two reviewers.

References

Amaro, T., Huvenne, V.A.I., Allcock, A.L., Aslam, T., Davies, J.S., Danovaro, R., De Stigter, H.C., Duineveld, G.C.A., Gambi, C., Gooday, A.J., Gunton, L.M., Hall, R., Howell, K.L., Ingels, J., Kiriakoulakis, K., Kershaw, C.E., Lavaleye, M.S.S., Robert, K., Stewart, H., Van Rooij, D., White, M., Wilson, A.M., 2016. The Whittard Canyon - A case study of submarine canyon processes. Progress in Oceanography 146, 38–57, doi:10.1016/j.pocean.2016.06.003.

Amaro, T., de Stigter, H., Lavaleye, M., Duineveld, G., 2015. Organic matter enrichment in the Whittard Channel; its origin and possible effects on benthic mega fauna. Deep-Sea Research I 102, 90–100, doi:10.1016/j.dsr.2015.04.014.

Baines, P.G., 1982. On internal tide generation models. Deep-Sea Research 29, 307–338.

Bell, T.H., 1975. Topographically-generated internal waves in the open ocean. Journal of Geophysical Research 80, 320–327.

Blumberg, A.F., Mellor, G.L., 1987. A description of a three-dimensional coastal ocean circulation model, in: Heaps, N.S. (Ed.), Three-Dimensional Coastal Ocean Models, Vol. 4, American Geophysical Union, Washington, DC. pp. 1–16.

Bourgault, D., Morsilli, M., Richards, C., Neumeier, U., Kelley, D.E., 2014. Sediment resuspension and nepheloid layers induced by long internal solitary waves shoaling orthogonally on uniform slopes. Continental Shelf Research 72, 21–33, doi:10.1016/j.csr.2013.10.019.

Cacchione, D.A., Wunsch, C., 1974. Experimental study of internal waves over a slope. Journal of Fluid Mechanics 66, 223–239.

Carter, G.S., 2010. Barotropic and baroclinic M_2 tides in the Monterey Bay region. Journal of Physical Oceanography 40, 1766–1783, doi:10.1175/2010JPO4274.1.

Carter, G.S., Fringer, O.B., Zaron, E.D., 2012. Regional models of internal tides. Oceanography 25, 56–65, doi:10.5670/oceanog.2012.42.

Carter, G.S., Gregg, M.C., 2002. Intense, variable mixing near the head of Monterey Submarine Canyon. Journal of Physical Oceanography 32, 3145–3165.

Carter, G.S., Merrifield, M.A., 2007. Open boundary conditions for regional tidal simulations. Ocean Modelling 18, 194–209, doi:10.1016/j.ocemod.2007.04.003.

ACCEPTED MANUSCRIPT

Carter, G.S., Merrifield, M.A., Becker, J.M., Katsumata, K., Gregg, M.C., Luther, D.S., Levine, M.D., Boyd, T.J., Firing, Y.L., 2008. Energetics of M_2 barotropic-to-baroclinic tidal conversion at the Hawaiian Islands. Journal of Physical Oceanography 38, 2205–2223, doi:10.1175/2008JPO3860.1.

Cummins, P.F., Oey, L.Y., 1997. Simulation of barotropic and baroclinic internal tides of Northern British Columbia. Journal of Physical Oceanography 27, 762–781.

Duros, P., Fontanier, C., Metzger, E., Pusceddu, A. Cesbron, F., de Stigter, H.C., Bianchelli, S., Danovaro, R., Jorissen, F.J., 2011. Live (stained) benthic foraminifera in the Whittard Canyon, Celtic margin (NE Atlantic). Deep-Sea Research I 58, 128–146, doi:10.1016/j.dsr.2010.11.008.

Egbert, G.D., Erofeeva, S.Y., 2002. Efficient inverse modeling of barotropic ocean tides. Journal of Atmospheric and Oceanic Technology 19, 183–204.

Egbert, G.D., Erofeeva, S.Y., Ray, R.D., 2010. Assimilation of altimetry data for nonlinear shallow-water tides: Quarter-diurnal tides of the Northwest European Shelf. Continental Shelf Research 30, 668–679, doi:10.1016/j.csr.2009.10.011.

Eriksen, C.C., 1982. Observations of internal wave reflection off sloping bottoms. Journal of Geophysical Research 87, 525–538.

Eriksen, C.C., Osse, T.J., Light, R.D., Wen, T., Lehman, T.W., Sabin, P.J., Ballard, J.W., Chiodi, A.M., 2001. Seaglider: a long-range autonomous underwater vehicle for oceanographic research. IEEE Journal of Oceanic Engineering 26, 424–436, doi:10.1109/48.972073.

Flather, R.A., 1976. A tidal model of the north-west European continental shelf. Memoires de la Societe Royale des Sciences de Liege 6, 141–164.

García Lafuente, J., Sarhan, T., Vargas, M., Vargas, J., Plaza, F., 1999. Tidal motions and tidally-induced fluxes through La Línea submarine canyon, western Alboran Sea. Journal of Geophysical Research 104, 3109–3119.

Garrett, C., Kunze, E., 2007. Internal tide generation in the deep ocean. Annual Review of Fluid Mechanics 39, 57–87, doi:10.1146/annurev.fluid.39.050905.110227.

Gill, A.E., 1982. Atmosphere-Ocean Dynamics. Academic Press.

Gordon, R.L., Marshall, N.F., 1976. Submarine canyons: internal wave traps? Geophysical Research Letters 3, 622–624.

Green, J.A.M., Simpson, J.H., Legg, S., Palmer, M.R., 2008. Internal waves, baroclinic energy fluxes and mixing at the European shelf edge. Continental Shelf Research 28, 937–950, doi:10.1016/j.csr.2008.01.014.

Gregg, M.C., Carter, G.S., Kunze, E., 2005. Corrigendum. Journal of Physical Oceanography 35, 1712–1715.

Gregg, M.C., Hall, R.A., Carter, G.S., Alford, M.H., Lien, R.C., Winkel, D.P., Wain, D.J., 2011. Flow and mixing in Ascension, a steep, narrow canyon. Journal of Geophysical Research 116, C07016, doi:10.1029/2010JC006610.

Hall, R.A., Alford, M.H., Carter, G.S., Gregg, M.C., Lien, R.C., Wain, D.J., Zhao, Z., 2014. Transition from partly standing to progressive internal tides in Monterey Submarine Canyon. Deep-Sea Research II 104, 164–173, doi:10.1016/j.dsr2.2013.05.039.

Hall, R.A., Aslam, T., Huvenne, V.A.I., 2017. Partly standing internal tides in a dendritic submarine canyon observed by an ocean glider. Deep Sea Research Part I 126, 73–84, doi:10.1016/j.dsr.2017.05.015.

Hall, R.A., Carter, G.S., 2011. Internal tides in Monterey Submarine Canyon. Journal of Physical Oceanography 41, 186–204, doi:10.1175/2010JPO4471.1.

Hall, R.A., Huthnance, J.M., Williams, R.G., 2011. Internal tides, nonlinear internal wave trains, and mixing in the Faroe-Shetland Channel. Journal of Geophysical Research 116, C03008, doi:10.1029/2010JC006213.

Hall, R.A., Huthnance, J.M., Williams, R.G., 2013. Internal wave reflection on shelf slopes with depth-varying stratification. Journal of Physical Oceanography 43, 248–258, doi:10.1175/JPO–D–11–0192.1.

Harris, P.T., Whiteway, T., 2011. Global distribution of large submarine canyons: Geomorphic differences between active and passive continental margins. Marine Geology 285, 69–86, doi:10.1016/j.margeo.2011.05.008.

Holt, J.T., Thorpe, S.A., 1997. The propagation of high frequency internal waves in the Celtic Sea. Deep-Sea Research I 44, 2087–2166.

Hopkins, J.E., Stephenson, G.R., Green, J.A.M., Inall, M.E., Palmer, M.R., 2014. Storms modify baroclinic energy fluxes in a seasonally stratified shelf sea: Inertial-tidal interaction. Journal of Geophysical Research: Oceans 119, 6863–6883, doi:10.1002/2014JC010011.

Hotchkiss, F.S., Wunsch, C., 1982. Internal waves in Hudson Canyon with possible geological implications. Deep-Sea Research 29, 415–442.

Huvenne, V.A.I., Tyler, P.A., Masson, D.G., Fisher, E.H., Hauton, C., Hühnerbach, V., Le Bas, T.P., Wolff, G.A., 2011. A picture on the wall: innovative mapping reveals cold-water coral refuge in submarine canyon. PLoS ONE 6, e28755, doi:10.1371/journal.pone.0028755.

Inall, M., Aleynik, D., Boyd, T., Palmer, M., Sharples, J., 2011. Internal tide coherence and decay over a wide shelf sea. Geophysical Research Letters 38, L23607, doi:10.1029/2011GL049943.

Johnson, M.P., White, M., Wilson, A., Würzberg, L., Schwabe, E., Folch, H., Allcock, A.L., 2013. A vertical wall dominated by *Acesta excavata* and *Neopycnodonte zibrowii*, part of a undersampled group of deep-sea habitats. PLoS ONE 8, e79917, doi:10.1371/journal.pone.0079917.

Kang, D., Fringer, O., 2010. On the calculation of available potential energy in internal wave fields. Journal of Physical Oceanography 40, 2539–2545, doi:0.1175/2010JPO4497.1.

Kelly, S.M., Nash, J.D., 2010. Internal-tide generation and destruction by shoaling internal tides. Geophysical Research Letters 37, L23611, doi:10.1029/2010GL045598.

Kunze, E., MacKay, C., McPhee-Shaw, E.E., Morrice, K., Girton, J.B., Terker, S.R., 2012. Turbulent mixing and exchange with interior waters on sloping boundaries. Journal of Physical Oceanography 42, 910–927, doi:10.1175/JPO–D–11–075.1.

Kunze, E., Rosenfeld, L.K., Carter, G.S., Gregg, M.C., 2002. Internal waves in Monterey Submarine Canyon. Journal of Physical Oceanography 32, 1890–1913.

Lee, I.H., Lien, R.C., Liu, J.T., Chuang, W.S., 2009. Turbulent mixing and internal tides in Gaoping (Kaoping) Submarine

ACCEPTED MANUSCRIPT

Canyon, Taiwan. Journal of Marine Systems 76, 383–396, doi:10.1016/j.jmarsys.2007.08.005.
Lueck, R.G., Osborn, T.R., 1985. Turbulence measurements in a submarine canyon. Continental Shelf Research 4, 681–698.
Martini, K.I., Alford, M.H., Nash, J.D., Kunze, E., Merrifield, M.A., 2007. Diagnosing a partly standing internal wave in Mamala Bay, Oahu. Geophysical Research Letters 34, L17604, doi:10.1029/2007GL029749.
Masson, D.G., Huvenne, V.A.I., de Stigter, H.C., Arzola, R.G., LeBas, T.P., 2011. Sedimentary processes in the middle Nazaré Canyon. Deep-Sea Research II 58, 2369–2387, doi:10.1016/j.dsr2.2011.04.003.
McPhee-Shaw, E.E., Kunze, E., 2002. Boundary layer intrusions from a sloping bottom: a mechanism for generation intermediate nepheloid layers. Journal of Geophysical Research 107, 3050, 10.1029/2001JC000801.
McPhee-Shaw, E.E., Sternberg, R.W., Mullenbach, B., Ogston, A.S., 2004. Observations of intermediate nepheloid layers on the northern California continental margin. Continental Shelf Research 24, 693–720, doi:10.1016/j.csr.2004.01.004.
Nash, J.D., Alford, M.H., Kunze, E., 2005. Estimating internal wave energy fluxes in the ocean. Journal of Atmospheric and Oceanic Technology 22, 1551–1570.
New, A.L., 1988. Internal tidal mixing in the Bay of Biscay. Deep-Sea Research 35, 691–709.
Niwa, Y., Hibiya, T., 2001. Numerical study of the spatial distribution of the M_2 internal tide in the Pacific Ocean. Journal of Geophysical Research 106, 22441–22449.
Petruncio, E.T., Rosenfeld, L.K., Paduan, J.D., 1998. Observations of the internal tide in Monterey Canyon. Journal of Physical Oceanography 28, 1873–1903.
Pingree, R.D., Mardell, G.T., New, A.L., 1986. Propagation of internal tides from the upper slopes of the Bay of Biscay. Nature 321, 154–158.
Porter, M., Inall, M.E., Hopkins, J.E., Palmer, M.R., Dale, A.C., Aleynik, D., Barth, J.A., Mahaffey, C., Smeed, D., 2016. Glider observations of enhanced deep water upwelling at a shelf break canyon: A mechanism for cross-slope carbon and nutrient exchange. Journal of Geophysical Research: Oceans 121, 7575–7588, doi:10.1002/2016JC012087.
Puig, P., Palanques, A., 1998. Nepheloid structure and hydrographic control on the Barcelona continental margin, northwestern Mediterranean. Marine Geology 149, 39–54.
Puig, P., Palanques, A., Guillén, J., El Khatab, M., 2004. Role of internal waves in the generation of nepheloid layers on the northwestern Alboran slope: implications for continental margin shaping. Journal of Geophysical Research 109, C09011, doi:10.1029/2004JC002394.
Rainville, L., Johnston, T.M.S., Carter, G.S., Merrifield, M.A., Pinkel, R., Worcester, P.F., Dushaw, B.D., 2010. Interference pattern and propagation of the M_2 internal tide south of the Hawaiian Ridge. Journal of Physical Oceanography 40, 311–325, doi:10.1175/2009JPO4256.1.
Reid, G., Hamilton, D., 1990. A reconnaissance survey of the Whittard Sea Fan, Southwestern Approaches, British Isles. Marine Geology 92, 69–86.
Robert, K., Jones, D.O.B., Tyler, P.A., Van Rooij, D., Huvenne, V.A.I., 2015. Finding the hotspots within a biodiversity hotspot: fine-scale biological predictions within a submarine canyon using high-resolution acoustic mapping techniques. Marine Ecology 36, 1256–1276, doi:10.1111/maec.12228.
Sharples, J., Moore, C.M., Hickman, A.E., Holligan, P.M., Tweddle, J.F., Palmer, M.R., Simpson, J.H., 2009. Internal tidal mixing as a control on continental margin ecosystems. Geophysical Research Letters 36, L23603, doi:10.1029/2009GL040683.
Shepard, F.P., Marshall, N.F., McLoughlin, P.A., 1974. Currents in submarine canyons. Deep-Sea Research 21, 691–706.
Stewart, H.A., Davies, J.S., Guinan, J., Howell, K.L., 2014. The Dangeard and Explorer canyons, South Western Approaches UK: Geology, sedimentology and newly discovered cold-water coral mini-mounds. Deep-Sea Research II 104, 230–244, doi:10.1016/j.dsr2.2013.08.018.
Thomsen, L., Gust, G., 2000. Sediment erosion thresholds and characteristics of resuspended aggregates on the western European continental margin. Deep-Sea Research 47, 1881–1897.
Thorpe, S.A., White, M., 1988. A deep intermediate nepheloid layer. Deep Sea Research 35, 1665–1671.
Vangriesheim, A., Khripounoff, A., Crassous, P., 2009. Turbidity events observed *in situ* along the Congo submarine channel. Deep-Sea Research II 56, 2208–2222, doi:10.1016/j.dsr2.2009.04.004.
Vlasenko, V., Stashchuk, N., 2015. Internal tides near the Celtic Sea shelf break: A new look at a well known problem. Deep-Sea Research I 103, 24–36, doi:10.1016/j.dsr.2015.05.003.
Vlasenko, V., Stashchuk, N., Inall, M.E., Hopkins, J.E., 2014. Tidal energy conversion in a global hot spot: On the 3-D dynamics of baroclinic tides at the Celtic Sea shelf break. Journal of Geophysical Research: Oceans 119, 6863–6883, doi:10.1002/2014JC010011.
Vlasenko, V., Stashchuk, N., Inall, M.E., Porter, M., Aleynik, D., 2016. Focusing of baroclinic tidal energy in a canyon. Journal of Geophysical Research: Oceans 121, 2824–2840, doi:10.1002/2015JC011314.
Wain, D.J., Gregg, M.C., Alford, M.H., Lien, R.C., Hall, R.A., Carter, G.S., 2013. Propagation and dissipation of the internal tide in upper Monterey Canyon. Journal of Geophysical Research 118, 4855–4877, doi:10.1002/jgrc.20368.
Waterhouse, A.F., MacKinnon, J.A., Musgrave, R.C., Kelly, S.M., Pickering, A., Nash, J., 2017. Internal tide convergence and mixing in a submarine canyon. Journal of Physical Oceanography 47, 303–322, doi:10.1175/JPO–D–16–0073.1.
van Weering, T., Koster, B., Heerwaardes, J., Thomsen, L., Viergutz, T., 2000. A new technique for long-term deep seabed studies. Sea Technology 41, 17–27.
Wilson, A.M., Kiriakoulakis, K., Raine, R., Gerritsen, H.D., Blackbird, S., Allcock, A.L., White, M., 2015a. Anthropogenic influence on sediment transport in the Whittard Canyon, NE Atlantic. Marine Pollution Bulletin 101, 320–329, doi:10.1016/j.marpolbul.2015.10.067.
Wilson, A.M., Raine, R., Mohn, C., White, M., 2015b. Nepheloid layer distribution in the Whittard Canyon, NE Atlantic Margin. Marine Geology 367, 130–142, doi:10.1016/j.margeo.2015.06.002.
Wunsch, C., Webb, S., 1979. The climatology of deep ocean internal waves. Journal of Physical Oceanography 9, 235–243.

ACCEPTED MANUSCRIPT

Zhao, Z., Alford, M.H., Lien, R.C., Gregg, M.C., Carter, G.S., 2012. Internal tides and mixing in a submarine canyon with time-varying stratification. Journal of Physical Oceanography 42, 2121–2142, doi:10.1175/JPO–D–12–045.1.

Zilberman, N.V., Becker, J.M., Merrifield, M.A., Carter, G.S., 2009. Model estimates of M_2 internal tide generation over Mid-Atlantic Ridge topography. Journal of Physical Oceanography 39, 2635–2651, doi:10.1175/2008JPO4136.1.

ACCEPTED MANUSCRIPT

ACCEPTED MANUSCRIPT

Highlights

- Internal tide simulated in a dendritic submarine canyon: the Whittard canyon system
- Internal tide generated along the Celtic Sea shelf break and within the canyon
- Internal tide topographically steered and focused by steep canyon bathymetry
- Decreasing bathymetric resolution reduces internal tide generation and dissipation

ACCEPTED MANUSCRIPT